

Iterative addition of finite Larmor radius effects to finite element models using wavelet decomposition

P Vallejos¹ , T Johnson¹ , R Ragona² , D Van Eester², B Zaar¹  and T Hellsten¹

¹Dept. of Fusion Plasma Physics, School of Electrical Engineering and Computer Science, KTH, SE-10044 Stockholm, Sweden

²Laboratory for Plasma Physics, LPP-ERM/KMS, Bruxelles, Belgium

E-mail: pablova@kth.se

Received 14 October 2019, revised 19 December 2019

Accepted for publication 23 January 2020

Published 16 March 2020



CrossMark

Abstract

Modeling the propagation and damping of electromagnetic waves in a hot magnetized plasma is difficult due to spatial dispersion. In such media, the dielectric response becomes non-local and the wave equation an integro-differential equation. In the application of RF heating and current drive in tokamak plasmas, the finite Larmor radius (FLR) causes spatial dispersion, which gives rise to physical phenomena such as higher harmonic ion cyclotron damping and mode conversion to electrostatic waves. In this paper, a new numerical method based on an iterative wavelet finite element scheme is presented, which is suitable for adding non-local effects to the wave equation by iterations. To verify the method, we apply it to a case of one-dimensional fast wave heating at the second harmonic ion cyclotron resonance, and study mode conversion to ion Bernstein waves (IBW) in a toroidal plasma. Comparison with a local (truncated FLR) model showed good agreement in general. The observed difference is in the damping of the IBW, where the proposed method predicts stronger damping on the IBW.

Keywords: Morlet wavelets, finite element method, ion cyclotron resonance heating, mode conversion, ion Bernstein waves

(Some figures may appear in colour only in the online journal)

1. Introduction

Modeling the propagation and damping of electromagnetic waves in a hot magnetized plasma is difficult due to spatial dispersion [1–4]. Spatial dispersion occurs when natural length scales are present in a medium. As a consequence, the dielectric response becomes non-local and the wave equation an integro-differential equation that is difficult to solve with common numerical methods [5–7].

In the application of RF heating and current drive in tokamaks [8], accounting for spatial dispersion is important in modeling codes. Parallel spatial dispersion is caused by the parallel velocity of the particles, and is important for Landau damping and the Doppler broadening of the ion cyclotron resonances. In the presence of a poloidal magnetic field, parallel spatial dispersion makes the dielectric tensor an integral operator [7]. In the perpendicular direction, the finite Larmor radius (FLR) of the gyrating particles causes spatial dispersion. FLR effects give rise to higher harmonic ion cyclotron damping, transit-time magnetic pumping (TTMP) and mode conversion [1, 2, 9, 10].

Common numerical tools for solving the wave equation include the finite element (FE) method and Fourier spectral methods. The FE method is efficient in solving the wave



Original content from this work may be used under the terms of the [Creative Commons Attribution 3.0 licence](https://creativecommons.org/licenses/by/3.0/). Any further distribution of this work must maintain attribution to the author(s) and the title of the work, journal citation and DOI.

equation and can be applied on complex geometries. The main disadvantage of the FE method is that it cannot account for the non-local character of the dielectric response. Fourier spectral methods can describe non-local effects by using Fourier bases, however, these methods are time consuming and require a large amount of computer memory.

Much effort has been devoted to develop modeling codes that can simulate the propagation and damping of RF waves in hot magnetized plasmas [11–18]. A common approach is to solve the wave equation in two dimensions and take advantage of axisymmetry in the toroidal direction. The advantage of axisymmetry is that the electric field can be Fourier decomposed toroidally and simulations can be performed for a single toroidal mode number at a time. In the radial and poloidal directions (or poloidal plane), the choice of discretization method varies between different modeling codes. The simplest approach is to apply a FE discretization in the poloidal plane. This method relies on algebraic approximations that remove the integral operators in the dielectric tensor, so that the wave equation becomes a partial differential equation (e.g. by neglecting the poloidal contribution to the parallel wave number) [16, 18]. One approach to include non-local effects due to parallel dispersion is to Fourier decompose in the poloidal direction and use a FE discretization in the radial direction [11, 12]. For this type of numerical scheme, FLR effects are typically included by expanding the dielectric tensor in the Larmor radius, where the first few terms are kept. Such approximations are sufficient to describe e.g. higher harmonic damping and mode conversion from the fast magnetosonic wave (or fast wave) to electrostatic waves, but are only valid when the Larmor radius of the gyrating ions is relatively small. Fourier spectral methods can solve the integro-differential wave equation without imposing any approximations [17]. However, these methods require massive computing power and are difficult to apply outside the plasma domain.

Research in development of new numerical schemes to include non-local effects using the FE method has been made and is available in the literature. In [19, 20], Sauter *et al* developed a method for solving the one-dimensional wave equation using a FE scheme, where FLR effects are included by employing a gyrokinetic approach. In [21], a numerical method called Gabor element method was developed, which was used to study a case of mode conversion from fast to slow waves. In this numerical method, the electric field is expanded into Gabor functions (note that Gabor functions are similar to Morlet wavelets used in the present work), which results in sparse matrices. In [22], Meneghini *et al* developed a two-dimensional FE model for lower hybrid waves in tokamaks. This method is based on a cold plasma model, where hot plasma effects are added by iterations to the most important dielectric tensor elements. A similar iterative algorithm in one dimension was developed by Green *et al* [23], where parallel non-local effects are evaluated by calculating particle orbits backward in time and added by iterations to the wave equation. Recently, an *iterative wavelet FE* scheme has been developed that is suitable for modeling RF heating of tokamak plasmas [24]. This numerical scheme was tested for

parallel dispersion in one dimension, where non-local effects were evaluated using wavelets and added to the wave equation by iterations.

In this paper, the main objective is to show that the iterative wavelet FE scheme can account for spatial dispersion caused by FLR effects in one dimension. We split the susceptibility operator into an algebraic susceptibility tensor and an induced current density term (where the latter quantity contains the integral operators). The wave equation is solved with a FE scheme using the algebraic susceptibility tensor, where the induced current density is represented as an inhomogeneous term. The contribution of the induced current density is added by using a fixed point iteration scheme based on *Anderson Acceleration* [25]. The induced current density is assumed to be zero for the first iteration. For subsequent iterations, the induced current density is evaluated using solutions from previous iterations. To account for the non-local character, the induced current density is evaluated in wavelet space [24, 26–29]. In this work, the *Morlet wavelet* was used to perform the wavelet decomposition. Morlet wavelets have several attractive features, such as having good convergence properties in the wavelet transform as well as being localized in both configuration and frequency space [30–32].

As an example, we will apply this method to a case of fast wave heating at the second harmonic ion cyclotron resonance, and study mode conversion to ion Bernstein waves (IBW) for different toroidal mode numbers. In this model, we use the hot susceptibility tensor for Maxwellian plasmas, including FLR effects. We show that the solution converges and that it is consistent with the hot plasma dispersion relation. The solution is also compared with the results from the TOMCAT code [33], which is a one-dimensional ion cyclotron resonance heating code.

The paper is structured as follows: the wave equation and susceptibility tensor are described in section 2; the continuous wavelet transform and the wavelet representation of the susceptibility tensor are described in section 3; the simulation results in section 4, and the discussion and conclusions in sections 5 and 6, respectively.

2. Wave equation and susceptibility tensor

In this section, we develop a one-dimensional model for ion cyclotron resonance heating in a toroidal plasma. We derive an expression for the wave equation that is suitable to be solved with the iterative wavelet FE scheme. Furthermore, we describe the boundary conditions and give expressions for the susceptibility model. The last sections describe the hot plasma dispersion relation and the energy equation.

2.1. Wave equation

The wave equation is given in a cylindrical coordinate system ($\mathbf{e}_R, \mathbf{e}_\phi, \mathbf{e}_Z$), where \mathbf{e}_R is the major radius direction, \mathbf{e}_ϕ the toroidal direction and \mathbf{e}_Z the vertical direction. We assume that the plasma response and geometry are axisymmetric (i.e.

the model accounts for toroidal curvature). The plasma is inhomogeneous in \mathbf{e}_R only and is invariant in \mathbf{e}_Z . We will also assume that the wave vector lies in the $R\phi$ plane (i.e. $k_Z = 0$). Under these assumptions, the wave equation can be written as [1, 2]

$$\nabla \times \nabla \times \mathbf{E} - \frac{\omega^2}{c^2} \left[\mathbf{I} + \sum_j \tilde{\chi}_j \right] \mathbf{E} = i\omega\mu_0 \mathbf{J}_{ext}, \quad (1)$$

where the tilde denotes integral operator, $\tilde{\chi}_j$ is the hot susceptibility operator for species j , \mathbf{I} the identity matrix and \mathbf{J}_{ext} the external current density. The solution has the form

$$\mathbf{E}(R, \phi) = \mathbf{E}_0(R) e^{in_\phi}, \quad (2)$$

where \mathbf{E}_0 is a complex amplitude, and n_ϕ is the toroidal mode number.

Let χ_j be an algebraic approximation to the susceptibility operator $\tilde{\chi}_j$. The relation between these two quantities can then be written as

$$\tilde{\chi}_j = \chi_j + \delta\tilde{\chi}_j, \quad (3)$$

where $\delta\tilde{\chi}_j$ is the difference and is an integral operator. Substituting the above expression for $\tilde{\chi}_j$ in equation (1) gives

$$\begin{aligned} \nabla \times \nabla \times \mathbf{E} - \frac{\omega^2}{c^2} \left[\mathbf{I} + \sum_j \chi_j \right] \mathbf{E} \\ = i\omega\mu_0 \mathbf{J}_{ext} + \frac{\omega^2}{c^2} \sum_j \delta\tilde{\chi}_j \mathbf{E}. \end{aligned} \quad (4)$$

The key point here is to represent the integral operator term as an inhomogeneous term on the right hand side of the wave equation. Furthermore, it is convenient to represent this term as an induced current density term, which we refer to as the *correction current*, given by

$$\delta\mathbf{J}_{ind} = -i\omega\epsilon_0 \sum_j (\tilde{\chi}_j - \chi_j) \mathbf{E}. \quad (5)$$

To solve equation (4), we iterate over $\delta\mathbf{J}_{ind}$ in a fixed point iteration scheme using Anderson Acceleration [24, 25]. Let k be the iteration index and $\mathbf{E}^{(0)} = \mathbf{0}$ the initial solution. A solution to the wave equation can then be found by solving the following equations,

$$\delta\mathbf{J}_{ind}^{(k)} = -i\omega\epsilon_0 \sum_j (\tilde{\chi}_j - \chi_j) \mathbf{E}^{(k)}, \quad (6)$$

$$\begin{aligned} \nabla \times \nabla \times \mathbf{E}^{(k+1)} - \frac{\omega^2}{c^2} \left[\mathbf{I} + \sum_j \chi_j \right] \mathbf{E}^{(k+1)} \\ = i\omega\mu_0 (\mathbf{J}_{ext} + \delta\mathbf{J}_{ind}^{(k)}). \end{aligned} \quad (7)$$

Thus, equation (7) can be solved using the FE method. To evaluate equation (6) and account for the non-local character of the equation, we use a method based on Morlet wavelet decomposition, which is described in section 3.

2.2. Boundary conditions to the wave equation

In this model, we assume that the domain is confined by perfectly conducting walls. Thus, the boundary condition

applied is

$$\mathbf{n} \times \mathbf{E} = \mathbf{0}, \quad (8)$$

where \mathbf{n} is the unit normal vector to the wall.

The antenna is located inside the domain and is represented as an internal boundary, where we assign a prescribed surface current density. In cylindrical coordinates, we let the antenna location be described by R_{ant} . The antenna surface current density \mathbf{J}_{ant} is then given by

$$\mathbf{J}_{ant}(R = R_{ant}, \phi, Z) = J_0 \mathbf{e}_Z, \quad (9)$$

where J_0 is a complex constant with the unit A m^{-1}

2.3. Hot susceptibility tensor

In this work, we use a quasi-homogeneous approximation of the susceptibility tensor, where we assume a slow variation in the density, temperature and magnetic field. The susceptibility tensor is given in a Cartesian coordinate system ($\mathbf{e}_x, \mathbf{e}_y, \mathbf{e}_z$), where the magnetic field is aligned in the positive \mathbf{e}_z direction and the wave vector is in the xz plane (i.e. $k_y = 0$). Denoting Fourier transformed variables using the hat symbol, the susceptibility tensor for a hot Maxwellian plasma is given by [1, 2]

$$\hat{\chi}_j^{(Stix)}(k_x, k_z) = \begin{bmatrix} \hat{\chi}_{xx,j} & \hat{\chi}_{xy,j} & \hat{\chi}_{xz,j} \\ -\hat{\chi}_{xy,j} & \hat{\chi}_{yy,j} & \hat{\chi}_{yz,j} \\ \hat{\chi}_{xz,j} & -\hat{\chi}_{yz,j} & \hat{\chi}_{zz,j} \end{bmatrix}, \quad (10)$$

where the elements are given by

$$\hat{\chi}_{xx,j} = \frac{\omega_{pj}^2 e^{-\lambda_j}}{\omega k_z v_j} \sum_{n=-\infty}^{\infty} \frac{n^2 I_n Z(\zeta_{n,j})}{\lambda_j}, \quad (11)$$

$$\hat{\chi}_{xy,j} = i\epsilon_j \frac{\omega_{pj}^2 e^{-\lambda_j}}{\omega k_z v_j} \sum_{n=-\infty}^{\infty} n(I_n - I_n') Z(\zeta_{n,j}), \quad (12)$$

$$\hat{\chi}_{yy,j} = \frac{\omega_{pj}^2 e^{-\lambda_j}}{\omega k_z v_j} \sum_{n=-\infty}^{\infty} \left[\frac{n^2 I_n}{\lambda_j} + 2\lambda_j (I_n - I_n') \right] Z(\zeta_{n,j}), \quad (13)$$

$$\hat{\chi}_{xz,j} = k_x \frac{\omega_{pj}^2 e^{-\lambda_j}}{\omega k_z \omega_{c,j}} \sum_{n=-\infty}^{\infty} \frac{n I_n Z'(\zeta_{n,j})}{\lambda_j}, \quad (14)$$

$$\hat{\chi}_{yz,j} = -i\epsilon_j k_x \frac{\omega_{pj}^2 e^{-\lambda_j}}{\omega k_z \omega_{c,j}} \sum_{n=-\infty}^{\infty} (I_n - I_n') \frac{Z'(\zeta_{n,j})}{2}, \quad (15)$$

$$\hat{\chi}_{zz,j} = -\frac{\omega_{pj}^2 e^{-\lambda_j}}{\omega k_z v_j} \sum_{n=-\infty}^{\infty} I_n \zeta_{n,j} Z'(\zeta_{n,j}), \quad (16)$$

where n is the harmonic number, ω_{pj} the plasma angular frequency, $\omega_{c,j}$ the cyclotron angular frequency, $\epsilon_j = q_j/|q_j|$ the charge sign, q_j the species charge, $\lambda_j = k_x^2 \rho_{L,j}^2/2$ the FLR parameter, $\rho_{L,j}$ is the Larmor radius, v_j the thermal velocity, $I_n = I_n(\lambda_j)$ the modified Bessel functions of order n , and $Z(\zeta_{n,j})$ the plasma dispersion function evaluated at $\zeta_{n,j} = (\omega + n\omega_{c,j})/(k_z v_j)$. The prime denotes derivative.

The magnetic field in tokamaks can be decomposed into toroidal and poloidal components. In this work, we neglect the contribution of the poloidal magnetic field in order to focus on FLR effects only. Such an assumption is reasonable, given that the poloidal magnetic field in general is much weaker than the

toroidal magnetic field. This assumption also simplifies the transformation matrix from the Cartesian coordinate system to the cylindrical coordinate system, and removes the integral operators due to parallel dispersion (the proposed numerical scheme was tested for parallel dispersion in [24]).

Since the wave equation is described in a cylindrical coordinate system, the susceptibility tensor must be transformed. Let \mathbf{e}_x be parallel to \mathbf{e}_R , \mathbf{e}_ϕ antiparallel to \mathbf{e}_z , and \mathbf{e}_y parallel to \mathbf{e}_z . Under this assumptions, the transformation matrix becomes

$$\mathbf{R} = \begin{bmatrix} 1 & 0 & 0 \\ 0 & 0 & -1 \\ 0 & 1 & 0 \end{bmatrix}, \quad (17)$$

and the transformed susceptibility tensor is given by

$$\hat{\chi}_j = \mathbf{R} \cdot \hat{\chi}_j^{(Stix)} \cdot \mathbf{R}^{-1}. \quad (18)$$

Without a poloidal magnetic field, the parallel wave number is antiparallel to the toroidal wave number. Hence, the parallel wave number becomes

$$k_z = -\frac{n_\phi}{R}. \quad (19)$$

2.4. Algebraic susceptibility tensor

The algebraic susceptibility tensor used here is based on the hot susceptibility tensor from previous subsection, but evaluated for the fast wave. This requires that the perpendicular wave number of the fast wave is known in advance [18]. The perpendicular wave number of the fast wave can be obtained from the following approximative dispersion relation

$$k_{FW}^2 \approx \frac{\omega^2}{c^2} \left[K_{xx} - n_z^2 + \frac{K_{xy}^2}{K_{xx} - n_z^2} \right]_{\lambda_j=0}, \quad (20)$$

where $K_{xx} = 1 + \sum_j \hat{\chi}_{xx,j}$, $n_z = ck_z/\omega$ is the parallel refractive index and $K_{xy} = \sum_j \hat{\chi}_{xy,j}$. An approximative algebraic susceptibility model can then be obtained by evaluating the hot susceptibility tensor for the fast wave, i.e.

$$\chi_j^{(Stix)} = \hat{\chi}_j^{(Stix)}(k_x = k_{FW}, k_z). \quad (21)$$

The main advantage of using this susceptibility tensor instead of a cold plasma model is that higher harmonic cyclotron damping, TTMP and Landau damping are described quite well for the fast wave.

2.5. Hot plasma dispersion equation

The local dispersion equation is obtained by setting the determinant of the Fourier transformed wave equation to zero (equation (1)). Using the Cartesian coordinate system, the dispersion equation is given by

$$\begin{aligned} D(n_x, n_z) = & (K_{xx} - n_z^2)((K_{yy} - n_x^2 - n_z^2)(K_{zz} - n_x^2) + K_{yz}^2) \\ & + K_{xy}(K_{xy}(K_{zz} - n_x^2) + K_{yz}(K_{xz} + n_z n_x)) \\ & + (K_{xz} + n_x n_z)(K_{xy} K_{yz} - (K_{yy} - n_x^2 - n_z^2) \\ & \times (n_z n_x + K_{xz})), \end{aligned} \quad (22)$$

where $\mathbf{K} = \mathbf{I} + \sum_j \hat{\chi}_j$, $n_x = ck_x/\omega$ and $n_z = ck_z/\omega$. The roots were calculated as the intersection of the contours $\text{Re}(D) = 0$ and $\text{Im}(D) = 0$ in the complex k_x plane.

2.6. Energy equation

For time harmonic waves in spatially dispersive media, the energy equation has the form

$$\nabla \cdot (\mathbf{S} + \mathbf{T}) = -P_{abs}, \quad (23)$$

where \mathbf{S} is the Poynting flux, \mathbf{T} the kinetic flux and P_{abs} is the local absorption. The Poynting flux is given by

$$\mathbf{S} = \frac{1}{2\mu_0} \text{Re}[\mathbf{E}^* \times \mathbf{B}]. \quad (24)$$

Expressions for the kinetic flux and the local absorption in inhomogeneous spatially dispersive media are given in [6, 34, 35]. In these expressions, the electric field is Fourier expanded and the kinetic flux and local absorption are calculated by using the *absorption kernel*. Due to the complexity of the theory, an equivalent expression based on Morlet wavelets has not been derived yet. In this work, we will use approximative expressions to evaluate the kinetic flux and the local absorption, which can be written as

$$\mathbf{T} \approx -\frac{\omega\epsilon_0}{4} \sum_j \mathbf{E}^* \cdot \frac{d\hat{\chi}_j^H}{d\mathbf{k}} \mathbf{E}, \quad (25)$$

$$P_{abs} \approx \frac{\omega\epsilon_0}{2} \sum_j \text{Im}[\mathbf{E}^* \cdot \hat{\chi}_j^A \mathbf{E}], \quad (26)$$

where $\hat{\chi}_j^H$ and $\hat{\chi}_j^A$ are the Hermitian and anti-Hermitian parts of the susceptibility tensor, respectively. In these expressions, the factors $\frac{d\hat{\chi}_j^H}{d\mathbf{k}} \mathbf{E}$ and $\hat{\chi}_j^A \mathbf{E}$ are evaluated using wavelet decomposition (i.e. non-locally). The electric field component \mathbf{E}^* on the left side of these factors is evaluated locally. Therefore, the evaluation becomes *non-symmetric*, and the results will only be approximative. However, for the fast wave, $\mathbf{T} \approx 0$, so that $\nabla \cdot \mathbf{P} \approx -P_{abs}$, and as such, this approximation should be reasonable. For the IBW, $\mathbf{P} \approx 0$, so that $\nabla \cdot \mathbf{T} \approx -P_{abs}$. Thus, the divergence of the kinetic flux of the IBW gives the local absorption.

3. Wavelets and the susceptibility tensor

In this section, we will start with a short description of the Morlet wavelet and the continuous wavelet transform, followed by a derivation of the susceptibility tensor in wavelet space. We also describe the wavelet grid, matched layers and how to discretize the wavelet scale parameter.

3.1. Morlet wavelet

Let $\psi(x)$ be the mother wavelet, which is a complex and continuously differentiable function. To generate a set of wavelets (or daughter wavelets) from the mother wavelet, we introduce the wavelet scale parameter a and the translation

parameter b . The set of wavelets is then given by [30–32]

$$\psi_{ab}(x) = \frac{1}{\sqrt{|a|}} \psi\left(\frac{x-b}{a}\right). \quad (27)$$

In this paper, we use the normalized complex Morlet wavelet that is defined as

$$\psi(x) = c_\sigma \pi^{-\frac{1}{4}} e^{-\frac{x^2}{2}} (e^{i\sigma x} - \kappa_\sigma), \quad (28)$$

where $\sigma = 6$ is a reference wave number and

$$\begin{aligned} \kappa_\sigma &= e^{-\frac{1}{2}\sigma^2}, \\ c_\sigma &= (1 + e^{-\sigma^2} - 2e^{-\frac{3}{4}\sigma^2})^{-\frac{1}{2}}. \end{aligned}$$

The central wave number of each Morlet wavelet is given by $k = \sigma/a$. The Fourier transformed Morlet wavelet is

$$\hat{\psi}_{ab}(k) = c_\sigma \sqrt{2} \pi^{\frac{1}{4}} |a|^{\frac{1}{2}} e^{-ikb} \left(e^{-\frac{(ak-\sigma)^2}{2}} - \kappa_\sigma e^{-\frac{(ak)^2}{2}} \right). \quad (29)$$

3.2. Continuous wavelet transform

The continuous wavelet transform of a continuously differentiable function $f(x)$ is [30, 36, 37]

$$f_{ab} = \mathbf{WT}[f(x)] = \int_{-\infty}^{\infty} f(x) \psi_{ab}^*(x) dx, \quad (30)$$

where $*$ denotes complex conjugate and $-\infty < a, b < \infty$ where $a \neq 0$. The inverse continuous wavelet transform returns the original function, given by

$$\begin{aligned} f(x) &= \mathbf{WT}^{-1}[f_{ab}](x) \\ &= \frac{1}{C_\psi} \int_{-\infty}^{\infty} \int_{-\infty}^{\infty} f_{ab} \psi_{ab}(x) \frac{dadb}{a^2}, \end{aligned} \quad (31)$$

where the admissibility constant is

$$C_\psi = \int_{-\infty}^{\infty} \frac{|\hat{\psi}(k)|^2}{|k|} dk < \infty. \quad (32)$$

3.3. Wavelet representation of the susceptibility tensor

As described in section 2.1, the considered plasma is assumed to be inhomogeneous in the \mathbf{e}_x direction only, and the wave vector to lie in the xz plane, i.e. $k_y = 0$. Under these circumstances, we can Fourier transform the susceptibility operator acting on the electric field in the \mathbf{e}_x direction as follows [6]

$$\tilde{\chi}_j \mathbf{E} = \frac{1}{2\pi} \int_{-\infty}^{\infty} \hat{\chi}_j(x, k_x, k_z) \hat{\mathbf{E}}(k_x, k_z) e^{ik_x x} dk_x. \quad (33)$$

Since the plasma is homogeneous and periodic in the toroidal direction, the susceptibility can be evaluated for one toroidal mode number at a time. We hereby drop the k_z dependence for simplicity in writing.

By rewriting the electric field as a Fourier transform, we obtain

$$\frac{1}{2\pi} \int_{k_x} \int_{x'} \hat{\chi}_j(x, k_x) \mathbf{E}(x') e^{ik_x(x-x')} dx' dk_x.$$

We can now wavelet decompose the electric field using equation (31). Furthermore, we note that the integral in x' is

the Fourier transform of the Morlet wavelet. The result is

$$\begin{aligned} &\frac{1}{2\pi} \frac{1}{C_\psi} \int_a \int_b \int_{k_x} \int_{x'} \hat{\chi}_j(x, k_x) \mathbf{E}_{ab} \psi_{ab}(x') e^{ik_x(x-x')} dx' dk_x \frac{dadb}{a^2} \\ &= \frac{1}{C_\psi} \int_a \int_b \mathbf{I}_{ab}(x) \mathbf{E}_{ab} \frac{dadb}{a^2}, \end{aligned} \quad (34)$$

where

$$\mathbf{I}_{ab}(x) = \frac{1}{2\pi} \int_{k_x} \hat{\chi}_j(x, k_x) \hat{\psi}_{ab}(k_x) e^{ik_x x} dk_x. \quad (35)$$

Next, we Taylor expand the susceptibility at $k_x = \sigma/a$

$$\begin{aligned} \mathbf{I}_{ab}(x) &= \sum_{p=0}^{\infty} \frac{1}{p!} \frac{\partial^p \hat{\chi}_j}{\partial k_x^p} \Big|_{k_x=\frac{\sigma}{a}} \\ &\frac{1}{2\pi} \int_{k_x} \left(k_x - \frac{\sigma}{a} \right)^p \hat{\psi}_{ab}(k_x) e^{ik_x x} dk_x, \end{aligned} \quad (36)$$

where p is the expansion order. Performing the integral over k_x requires some technical steps presented in appendix. The result is

$$\mathbf{I}_{ab}(x) = \chi_{j,ab}(x) \psi_{ab}(x), \quad (37)$$

where $\chi_{j,ab}$ is the susceptibility represented in wavelet space given by

$$\begin{aligned} \chi_{j,ab}(x) &= \sum_{p=0}^{\infty} \frac{i^p \text{He}_p(X_{ab})}{p! a^p} \frac{\partial^p \hat{\chi}_j}{\partial k_x^p} \Big|_{k_x=\frac{\sigma}{a}}, \\ X_{ab} &= \frac{x-b}{a}, \end{aligned} \quad (38)$$

where He_p are the probabilists Hermite polynomials [38]. Substituting into equation (33) gives the following result,

$$\tilde{\chi}_j \mathbf{E} = \mathbf{WT}^{-1}[\chi_{j,ab} \mathbf{E}_{ab}](x). \quad (39)$$

Equation (39) implies that the non-local susceptibility response can be evaluated by multiplying the susceptibility and electric field in wavelet space, and then performing the inverse wavelet transform.

3.4. Evaluation of the correction current

To evaluate the correction current, we use equation (39) in (6), which gives

$$\delta \mathbf{J}_{ind}^{(k)} = -i\omega\epsilon_0 \sum_j \mathbf{WT}^{-1}[(\chi_{j,ab} - \chi_j) \mathbf{E}_{ab}^{(k)}](x), \quad (40)$$

where

$$\mathbf{E}_{ab}^{(k)} = \mathbf{WT}[\mathbf{E}^{(k)}(x)], \quad (41)$$

is the wavelet transform of the electric field.

3.5. The wavelet grid and matched layers

It is not necessary to evaluate $\delta \mathbf{J}_{ind}$ over the whole domain used in the FE discretization. The FLR effects are important where the plasma is hot, whereas in regions with low temperature the FLR effects are expected to be small. It is therefore convenient to define a smaller grid for the evaluation of $\delta \mathbf{J}_{ind}$

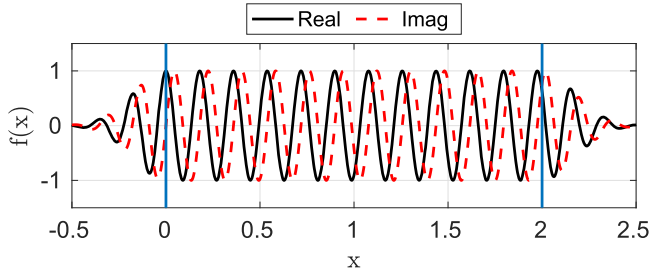


Figure 1. Illustration of matched layers. The function $f(x) = e^{ikx}$ with $k = 35$ is defined over the interval $0 \leq x \leq 2$. Matched layers are applied at $-0.5 \leq x \leq 0$ and $2 \leq x \leq 2.5$ and the function $f(x)$ is matched with Morlet wavelets with similar wave number.

in order to reduce the computational cost. This grid is called the *wavelet grid*.

Another complication occurs when a finite wavelet grid is used in the continuous wavelet transform, which is defined on an infinite interval. The introduction of a finite grid results in *edge artifacts* when performing the wavelet transform. These artifacts occur when the wavelets are near the boundaries, so that information outside the finite interval is required. In many applications, this is solved to some degree by using extension methods, which include zero padding, symmetric and periodic extensions [39, 40]. In this work, we solve this issue by using a technique called *matched layers* at the boundaries of the wavelet grid [24, 26]. This is basically an extension method where the function of interest is extended by matching it with a Morlet wavelet with similar wave number (see figure 1). The method ensures that the function becomes continuous over the boundary and that all edge artifacts in the wavelet transform fall within the matched layers. The evaluation of $\delta\mathbf{J}_{ind}$ is therefore performed in the extended wavelet grid. The matched layers are then removed on the correction current before solving the wave equation.

3.6. Scale parameter and admissibility constant

The scale parameter a is assumed to be continuous in the wavelet transform. In order to perform the calculations numerically, the scale parameter must be discretized. The calculations in this paper are based on a discretized scale parameter given by

$$a = 2^{m/4}, \quad (42)$$

where m is an integer. The constant C_ψ in equation (31) depends on the discretization and have been numerically calculated to be $C_\psi \approx 1.1598$.

4. Fast wave heating and mode conversion

To test the proposed numerical scheme, the code FEMIC1D was developed in MATLAB[®]. In FEMIC1D, the wave equation was solved using the RF module in COMSOL Multiphysics[®], while the evaluation of equation (6) was performed in MATLAB[®]. The interface between COMSOL Multiphysics[®] and MATLAB[®] was handled using the LiveLink[™] for MATLAB[®].

Table 1. Summary of the model parameters.

Parameter	Value
Magnetic field, B_0	1.70 T
Major radius, R_0	2.97 m
Toroidal mode, n_ϕ	15, 20, 27
Antenna frequency	49 MHz
Antenna position	3.95 m
Wall, low field side	4.08 m
Wall, high field side	1.80 m
Mesh size, plasma	0.50 mm
Mesh size, SOL	5.00 mm

The model parameters, summarized in table 1, were chosen to mimic a JET-like scenario. We considered a pure hydrogen plasma, where the antenna frequency and magnetic field were tuned for second harmonic heating of hydrogen ions near the magnetic axis. We included up to 8 harmonics in the susceptibility tensor (equation (10)), and four terms in the wavelet representation of the susceptibility tensor (equation (38)). The toroidal magnetic field was given by

$$B_{tor} = \frac{B_0 R_0}{R}, \quad (43)$$

where B_0 is the on-axis magnetic field and R_0 is the major radius. The density and temperature profiles are shown in figure 2. For simplicity, flat profiles were assumed in the plasma with a smooth transition over the pedestal to the low-density domain (or scrape-off-layer). The pedestal was described by an *mtanh* model [18]. The electron density in the low-density domain was $n_{SOL} = 4.2 \cdot 10^{17} \text{ m}^{-3}$, the electron temperature $T_{e,SOL} = 23 \text{ eV}$, and the ion temperature $T_{i,SOL} = 16 \text{ eV}$.

To solve the wave equation using the FE method, a grid size of 0.5 mm was applied in the plasma domain and 5.0 mm in the low-density domains. Second order elements were used. The wavelet grid was defined between $1.96 \leq R \leq 3.84 \text{ m}$, with a grid step of 0.63 mm. The scale parameter was chosen so that wave numbers ranging between 20 and 1536 m^{-1} were resolved.

The model with $n_\phi = 15$ required a wavelet grid with finer resolution. The step was set to 0.54 mm and modes with wave numbers between 20 and 1827 m^{-1} were resolved.

4.1. Dispersion relation

The dispersion relation for $n_\phi = 20$ is shown in figure 3(a). The fast wave branch has wave numbers ranging between $30 \leq k_x \leq 65$ in the plasma, and is evanescent in the low-density regions. Its imaginary component indicates that the second harmonic ion cyclotron resonance is located at $R = 3.1 \text{ m}$. A mode conversion zone can be identified at the resonance, where the dispersion relations of the fast wave and the IBW intersect. The IBW propagates in the negative major radius direction and becomes strongly damped near $R \approx 2.2 \text{ m}$. Note that the imaginary component of k_x for the IBW is negative, indicating that the wave is backward propagating

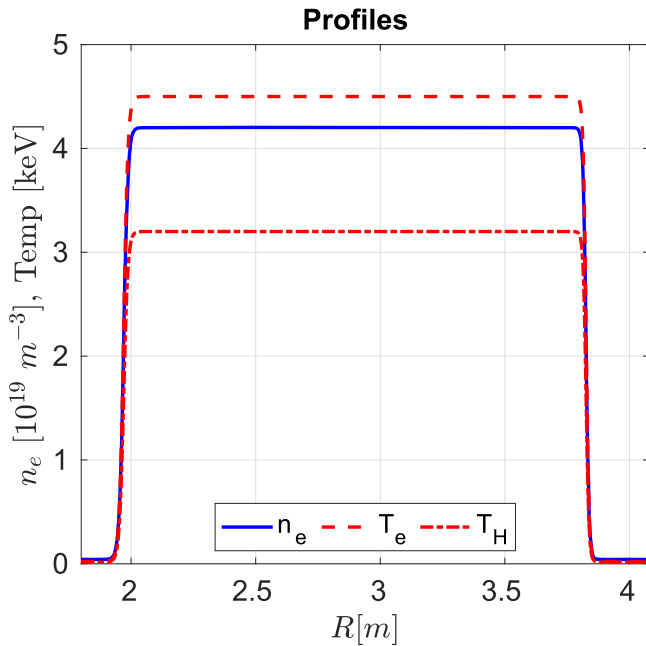


Figure 2. Density and temperature profiles.

(i.e. the phase and group velocity are in opposite directions). A third branch is observed near $R \approx 3.8$ m, which is an IBW associated with the third harmonic ion cyclotron resonance. However, this wave was not excited in the plasma and will not be discussed further.

Figure 3(b) shows the dispersion relations for the IBW for the toroidal mode numbers 15, 20 and 27. The real parts of the dispersion relations are only weakly dependent on the toroidal mode number. In contrast, the imaginary part defining the damping location is sensitive to the toroidal mode number. The lower the toroidal mode number, the longer distance the IBW can propagate from the second harmonic cyclotron resonance before being strongly damped.

4.2. Electric field for $n_\phi = 20$

The solution to the wave equation for $n_\phi = 20$ as predicted by FEMIC1D is shown in figure 4. The incoming fast wave couples to the plasma and propagates in the negative major radius direction. The wave becomes damped when crossing the ion cyclotron resonance near $R = 3.1$ m, which we identify as a reduction of the wave amplitude (there is also a weak change in the amplitude due to the change in the toroidal magnetic field). The fast wave is reflected at the pedestal near $R \approx 2.0$ m and crosses the second harmonic cyclotron resonance a second time.

The fast wave is partly converted to IBWs when crossing the second harmonic cyclotron resonance. The presence of the IBW is only observed in the E_R and E_ϕ components as a short wavelength mode, which is a typical feature of electrostatic waves [41]. Figure 5 shows the propagation and damping of the IBW, which was obtained by filtering the electric field using wavelets. The IBW is born near the second harmonic cyclotron resonance and propagates in the negative major radius direction. We note that the E_ϕ component of the IBW

increases when propagating away from the resonance. On the other hand, the E_R component increases rapidly at the resonance and varies weakly when propagating away from the resonance. Thus, since electron Landau damping is quadratic in the amplitude of E_ϕ , the damping of the IBW becomes stronger. When the wave crosses $R \approx 2.4$ m, it becomes strongly damped and vanishes. This behavior is consistent with the hot plasma dispersion relation in figure 3.

The amplitude of the wavelet coefficients of the E_R component is shown in figure 6. The incoming fast wave branch is seen in the lower half of the spectrogram, which corresponds to waves with negative wave number. The ion cyclotron damping at $R \approx 3.1$ m can be identified as a reduction of the amplitude of the wavelet coefficients. At the plasma edge near $R \approx 2.0$ m, we can observe that the fast wave is reflected (due to the cutoff) and reappears in the upper half of the spectrogram. The IBW branch is here only seen in the upper half, which corresponds to waves with positive wave numbers. However, since the IBW propagates in the negative major radius direction (i.e. negative group velocity), this is yet another indication that the wave is backward propagating.

In figure 7, the electric field components as predicted by TOMCAT are shown. By comparing the E_Z component in figure 7(b) with figure 4(c), we find good qualitative agreement between FEMIC1D and TOMCAT, which indicates that the description of the fast wave is similar. By comparing the E_R components in figures 7(a) and 4(a), we observe good agreement for the fast wave only. The main difference is the propagation and damping of the IBW. The characteristic of the IBW as predicted by TOMCAT is shown in figure 8. Near the second harmonic resonance, we observe a similar behavior between the two codes. When propagating away from the second harmonic resonance, the amplitude in E_R stays constant down to the plasma edge. As for the E_ϕ component, we note that its amplitude grows as it propagates away from the resonance. However, despite that E_ϕ is growing, the electron Landau damping does not damp out the wave. We also note that the amplitude of the IBW near the resonance in TOMCAT is about a factor two larger than in FEMIC1D, indicating a larger fraction of mode conversion. A possible explanation is that the interference patterns caused by the incoming and reflected fast waves are different in FEMIC1D and TOMCAT. As was shown in [42], the mode conversion rate is sensitive to these interference patterns.

4.3. Power absorption

The total power absorption P_{abs} and absorption profiles were calculated assuming unit current density in the antenna strap. Since we have a one-dimensional axisymmetric model where the solution is invariant in the \mathbf{e}_z direction, the total power absorption was estimated by integrating the power absorption density in the $R\phi$ plane (i.e. P_{abs} has the unit W m^{-1}). The results are summarized in table 2 and show that the absorbed power increases with decreasing toroidal mode number. This behavior is consistent with both theoretical predictions and experiments [18, 43, 44]. Furthermore, both FEMIC1D and

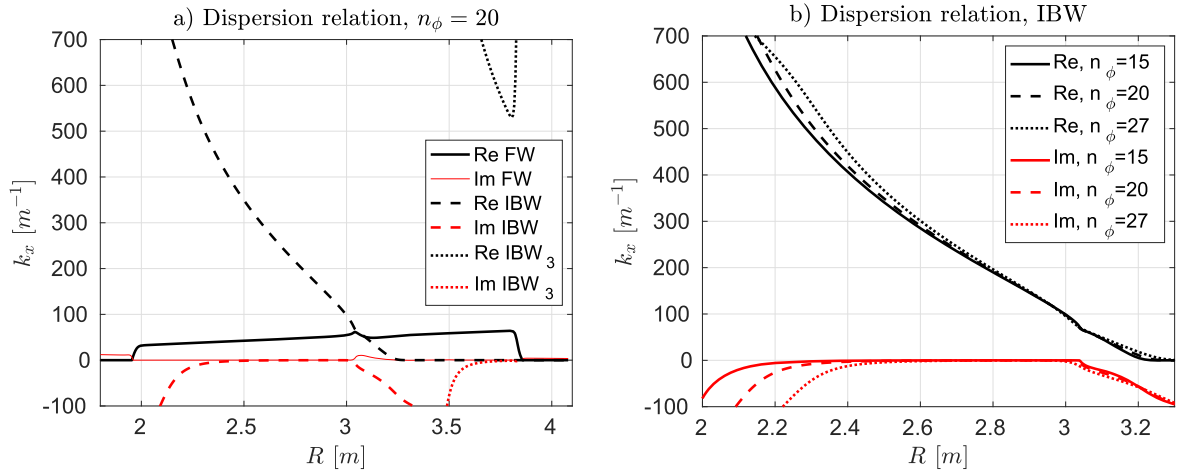


Figure 3. (a) Dispersion relations for $n_\phi = 20$. Black and red curves represent the real and imaginary parts, respectively. The solid line represents the fast wave, the dashed line the IBW, and the dotted line the IBW related to the third harmonic ion cyclotron resonance. (b) Dispersion relations for the IBW for toroidal mode numbers 15, 20 and 27. Real parts are represented in black, imaginary parts in red.

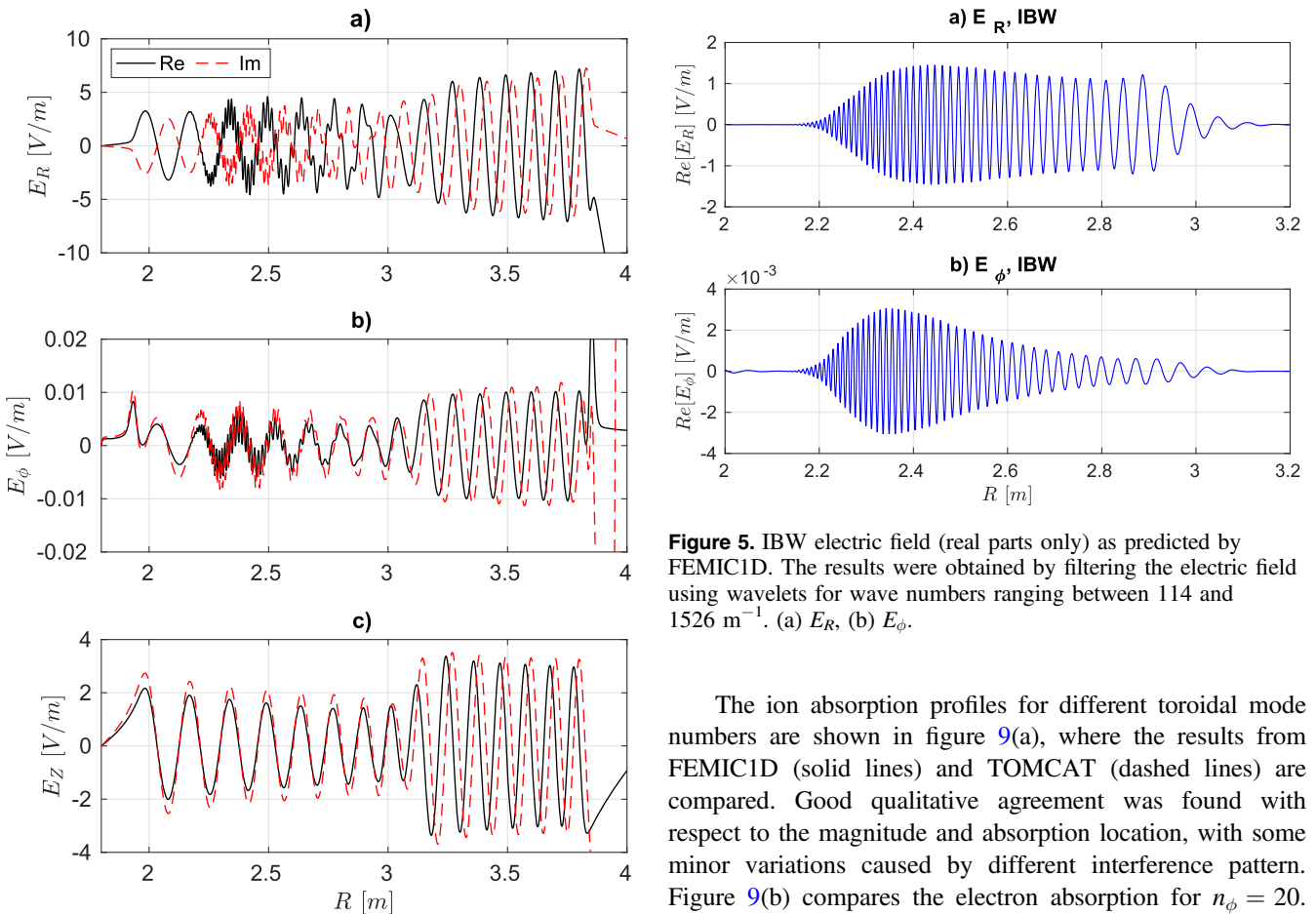


Figure 4. Electric field calculated by FEMIC1D for the case with $n_\phi = 20$. Real parts are drawn in black and imaginary parts in red. (a) E_R , (b) E_ϕ and (c) E_z .

TOMCAT predict that the electron power partition increases with the toroidal mode number, while the hydrogen power partition decreases. This is due to stronger electron absorption with increasing toroidal mode number [9, 10, 45].

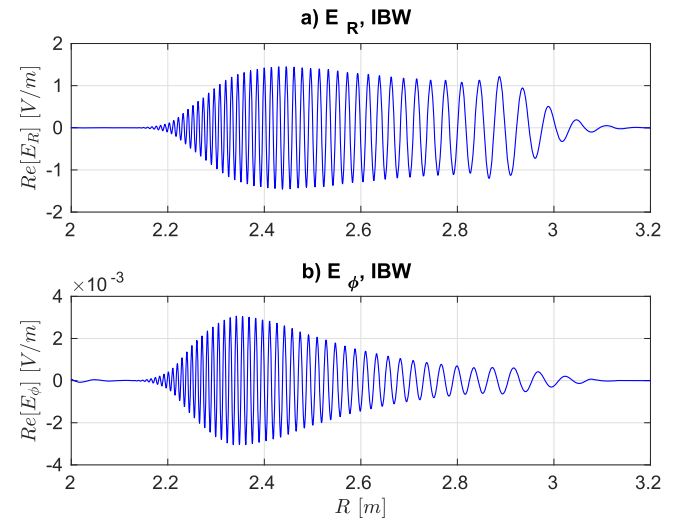


Figure 5. IBW electric field (real parts only) as predicted by FEMIC1D. The results were obtained by filtering the electric field using wavelets for wave numbers ranging between 114 and $1526 m^{-1}$. (a) E_R , (b) E_ϕ .

The ion absorption profiles for different toroidal mode numbers are shown in figure 9(a), where the results from FEMIC1D (solid lines) and TOMCAT (dashed lines) are compared. Good qualitative agreement was found with respect to the magnitude and absorption location, with some minor variations caused by different interference pattern. Figure 9(b) compares the electron absorption for $n_\phi = 20$. Two important observations can be made. First, the difference in the interference patterns is also observed in the electron absorption profiles. Second, TOMCAT predicts higher electron absorption in the interval $2.0 \leq R \leq 2.3$ m. The difference is due to the IBW damping. In FEMIC1D, the IBW is completely absorbed at $R = 2.2$ m. In contrast, the weaker damping in TOMCAT allows the IBW to propagate to the plasma edge at $R = 2.0$ m, which increases the total electron damping in the interval $2.0 < R < 2.3$ m. A similar behavior

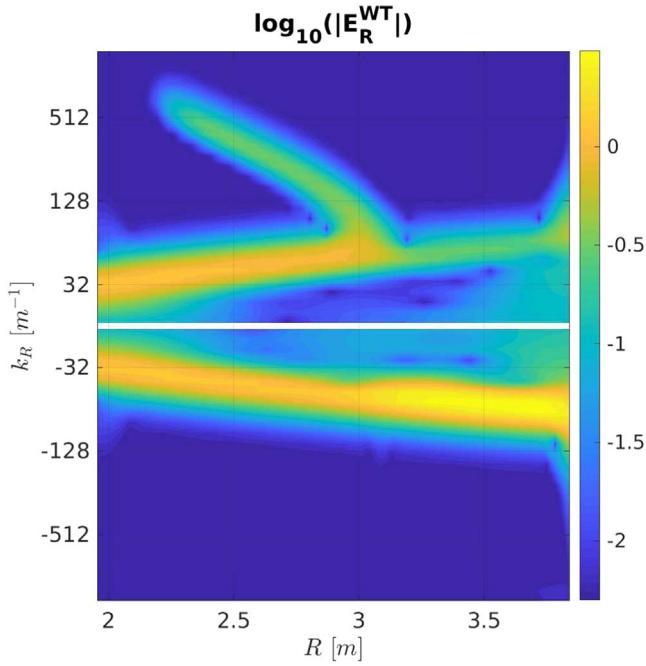


Figure 6. Absolute value of the wavelet coefficients of the E_R component, where $k_R = 6/a$.

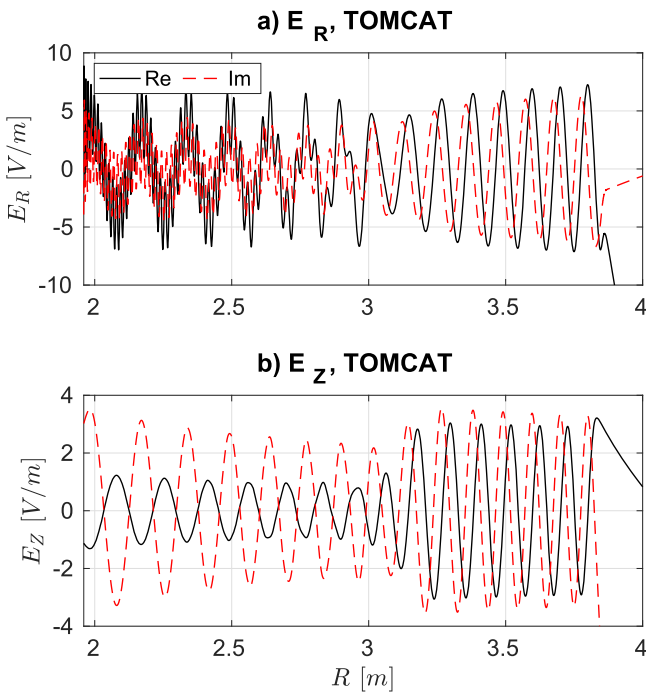


Figure 7. Electric field as predicted by the TOMCAT code for $n_\phi = 20$. Real parts are drawn in black and imaginary parts in red. (a) E_R , (b) E_Z .

was observed for the other toroidal mode numbers, which are not shown here for brevity.

The electron absorption is described by TTMP and electron Landau damping. For the fast wave, these two absorption mechanisms are coherent and connected by the susceptibility elements $\hat{\chi}_{yz,e}$ and $\hat{\chi}_{zy,e}$. This is illustrated in

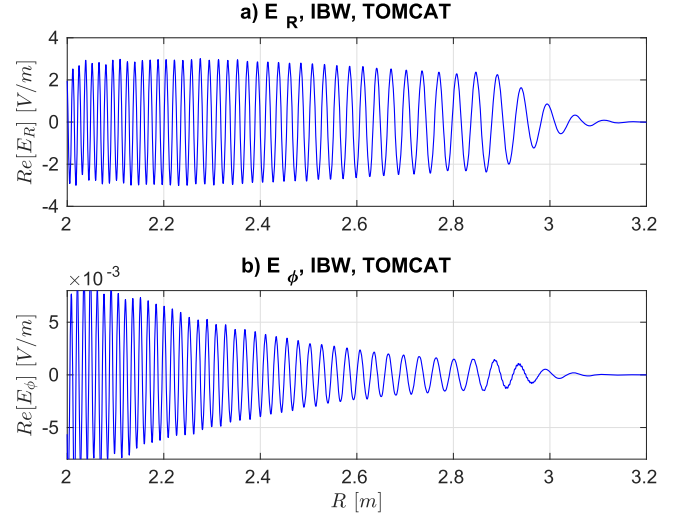


Figure 8. Electric field (real parts only) of the IBW as predicted by the TOMCAT code. The results were obtained by filtering the electric field using wavelets for wave numbers ranging between 114 and 1526 m^{-1} . (a) E_R , (b) E_ϕ .

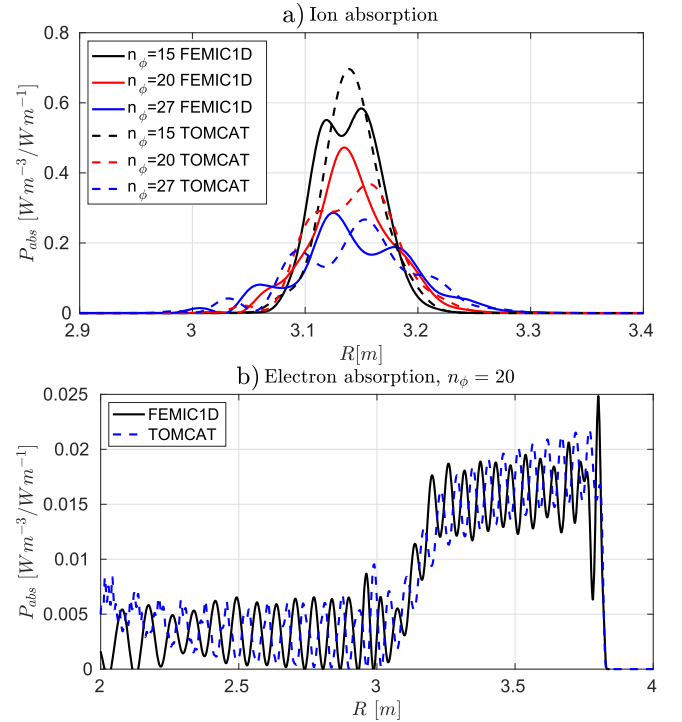


Figure 9. Power absorption profiles as predicted by FEMIC1D (solid lines) and TOMCAT (dashed lines). (a) Ions absorption for different toroidal mode numbers, (b) electrons absorption for $n_\phi = 20$.

figure 10 for the case with $n_\phi = 20$. Both the TTMP and electron Landau damping are positive definite, where the TTMP is a factor of two larger. The contribution of the cross terms is negative definite and roughly cancels the contribution of the TTMP, which leaves a net absorption similar to the electron Landau damping [1, 45].

Figure 11 shows the absorption profiles of the IBW for different toroidal mode numbers, as predicted by FEMIC1D. The location of the maximum absorption is dependent on the

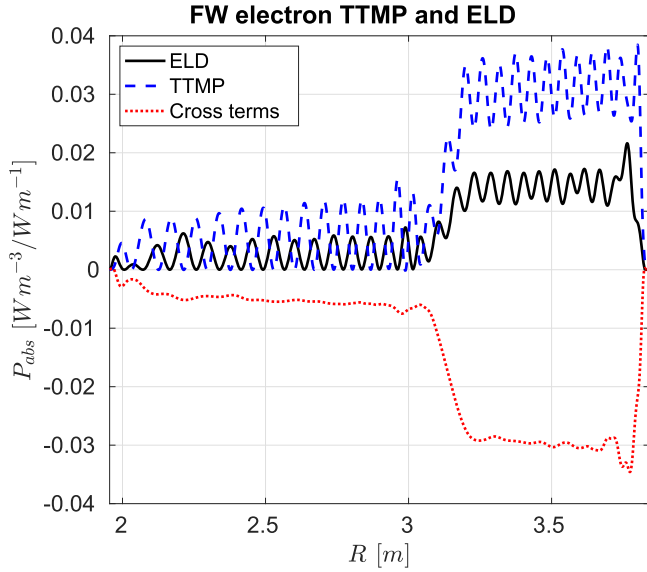


Figure 10. Electron Landau damping (black solid line), transit time magnetic pumping (blue dashed line) and the cross terms (red dotted line) as predicted by FEMIC1D for $n_\phi = 20$. The electron Landau damping is given by $\frac{1}{2}\omega\epsilon_0 \text{Im}(E_z^* \hat{\chi}_{z,e}^A E_z)$, TTMP by $\frac{1}{2}\omega\epsilon_0 \text{Im}(E_y^* \hat{\chi}_{y,e}^A E_y)$ and the cross terms by $\frac{1}{2}\omega\epsilon_0 \text{Im}(E_y^* \hat{\chi}_{y,z,e}^A E_z + E_z^* \hat{\chi}_{z,y,e}^A E_y)$.

Table 2. Total power absorption P_{abs} and the power partitions p_H and p_e for different toroidal mode numbers as predicted by FEMIC1D. The power partitions p_H^{TOMCAT} and p_e^{TOMCAT} as predicted by the TOMCAT code are also shown.

n_ϕ	P_{abs}	p_H	p_e	p_H^{TOMCAT}	p_e^{TOMCAT}
15	31.4 W m ⁻¹	87.5%	12.5%	81.9%	18.1%
20	20.7 W m ⁻¹	70.5%	29.5%	68.5%	31.5%
27	13.5 W m ⁻¹	56.5%	43.5%	57.1%	42.9%

toroidal mode number. The lower the toroidal mode number, the further the IBW propagates before being damped. Similar conclusions can be drawn by studying the kinetic flux of the IBW in figure 12, where we also observe that the kinetic flux decreases as the wave propagates in the negative major radius direction. In these calculations, the total electron absorption of the IBW amounted to 0.63%, 0.44% and 0.21% of the total absorbed power for the toroidal mode numbers 15, 20 and 27, respectively. Thus, the fraction of mode conversion increases for lower toroidal mode numbers.

Since the IBW is an electrostatic wave, its Poynting flux is negligible. Therefore, the local absorption P_{abs} is balanced by the divergence of the kinetic flux $\nabla \cdot \mathbf{T}$. This is illustrated in figure 13, which shows that these two quantities balance each other in the interval $2.2 \leq R \leq 2.5$ m.

4.4. The correction current

The algebraic susceptibility χ_j in equation (7) can describe the physics of the fast wave quite well (including some FLR effects of the fast wave). However, this susceptibility model

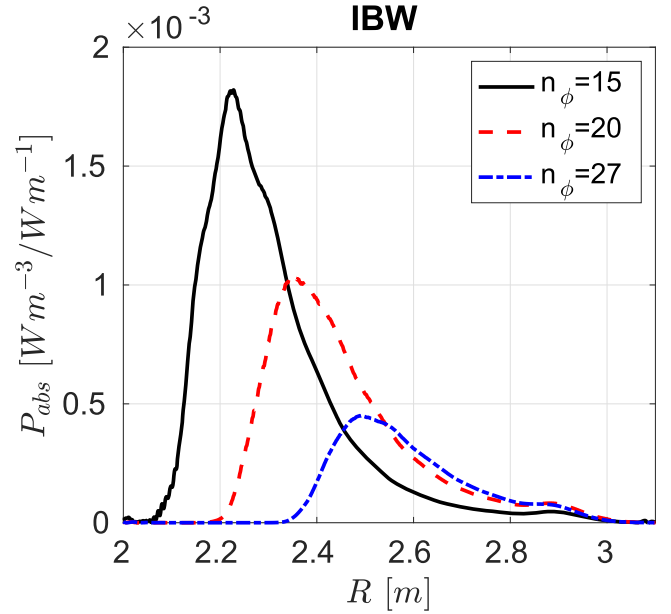


Figure 11. Electron absorption profiles for IBW for different toroidal mode numbers as predicted by FEMIC1D. The results were calculated using wavelet filtered electric fields.

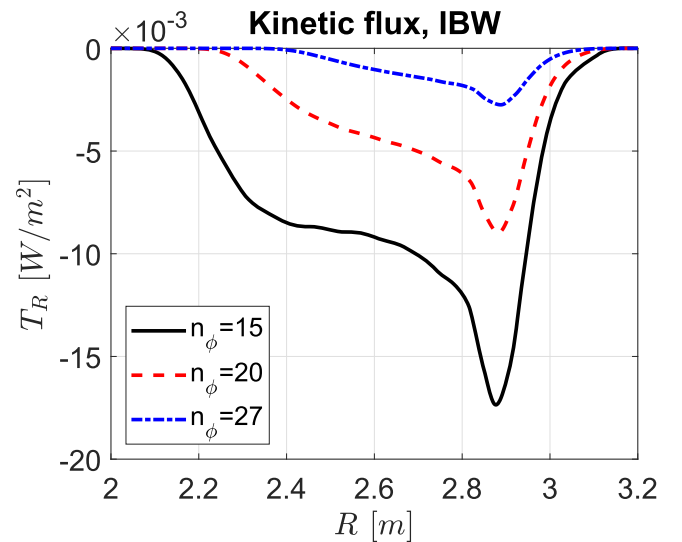


Figure 12. Kinetic flux for IBW for different toroidal mode numbers as predicted by FEMIC1D. The results were calculated using wavelet filtered electric fields.

cannot describe the physics related to non-local effects, in particular, the mode conversion and the propagation and damping of the IBW. These effects, which are completely missing in the algebraic susceptibility model, are described by the correction current $\delta \mathbf{J}_{ind}$.

Figure 14 shows the components of the correction current. The oscillation and amplitude variations in δJ_x and δJ_y correlates with the oscillations of the IBW. The wavelet spectrogram of the δJ_x component is shown in figure 15(a), which is useful in order to further understand the behavior of the correction current (the wavelet spectrogram for δJ_y shows similar information and is not shown for brevity). In the spectrogram, we can see that the wavelet bases that contribute

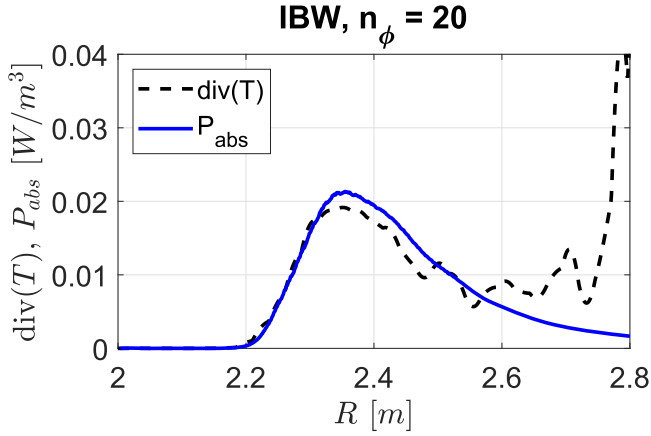


Figure 13. Comparison between $\nabla \cdot \mathbf{T}$ and P_{abs} for the IBW for the toroidal mode number 20. Far away from the mode conversion zone, the Poynting flux of the IBW is negligible, thus the local absorption is balanced by $\nabla \cdot \mathbf{T}$.

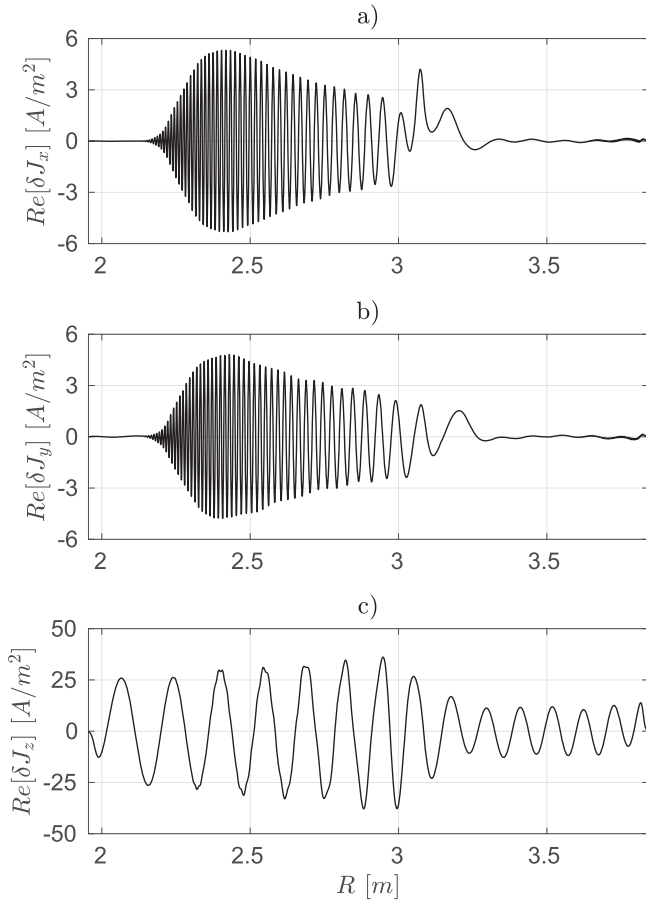


Figure 14. Real part of the correction current in FEMIC1D for the last iteration for $n_\phi = 20$. (a) δJ_x , (b) δJ_y , (c) δJ_z .

to the induced current density coincide quite well with the wavelet bases of the IBW in figure 6. Another interesting point is that the wavelet bases related to the fast wave branch range from very small to negligible. This indicates that the algebraic susceptibility model is a good approximation to describe the propagation and damping of the fast wave, as the

correction current does not add any significant corrections to the fast wave.

The parallel current density component δJ_z is shown in figure 14(c), and its wavelet spectrogram in figure 15(b). This component adds corrections to both the fast wave and the IBW. The corrections for the IBW are related to the $\hat{\chi}_{zz,j}$ component and are rather small. This is expected, since the dependence of k_R in the $\hat{\chi}_{zz,j}$ is very weak. In contrast, large amplitude corrections for the fast wave are observed. These corrections are also caused by FLR effects, and affects the fast wave polarization of the wave in the yz plane. The effect originates from the susceptibility element $\hat{\chi}_{zy,j} = -\hat{\chi}_{yz,j}$, where the fast wave polarization is described by $E_z/E_y \approx -\hat{\chi}_{zy,j}/\hat{\chi}_{zz,j}$ [45] (a similar effect is caused by the $\hat{\chi}_{zx,j}$ term, but is negligible here). Since $\hat{\chi}_{zy,j}$ is proportional to the wave number k_x , the response is dependent on the sign of the wave number, which causes the effect. However, this effect does not modify the power absorption, since the cross term in the power kernel, $E_z \hat{\chi}_{zy,j}^A E_y$, becomes an even function of k_x (the superscript A denotes the anti-Hermitian part). Thus, calculations that do not account for this FLR effect may still obtain a reasonable power balance.

4.5. Convergence

The residual norm is based on the electric field components in the Anderson Acceleration routine, which is given by

$$f = \|\mathbf{E}^{(k)} - \mathbf{E}^{(k-1)}\|. \quad (44)$$

Convergence is achieved when the residual norm f is smaller than the absolute tolerance, which is set to 10^{-3} . The evolution of the convergence is shown in figure 16. Overall, as long as the FE and wavelet grids have good resolutions, the Anderson Acceleration fixed point iteration scheme exhibits good convergence properties. However, the number of iterations to achieve convergence vary significantly. It was found that the number of iterations required for convergence are related to the number of oscillations in the correction current. Hence, the longer distance the IBW propagates, the more oscillations will be required in the correction current, which increases the number of iterations.

5. Discussion

In general, the propagation and damping of the fast wave as predicted by the FEMIC1D code is consistent with the predictions of the TOMCAT code. The observed difference is the damping of the IBW, where FEMIC1D predicts stronger electron Landau damping compared with TOMCAT. The reason behind this is that the FEMIC1D code has an all order FLR description of the dielectric tensor, while the TOMCAT code uses a truncated FLR expansion. A truncated FLR expansion works well when the Larmor radius of the hydrogen population is small, i.e. $\lambda_H \ll 1$. This model works well for the fast wave and for modeling mode conversion. However, as the wave propagates away from the mode conversion

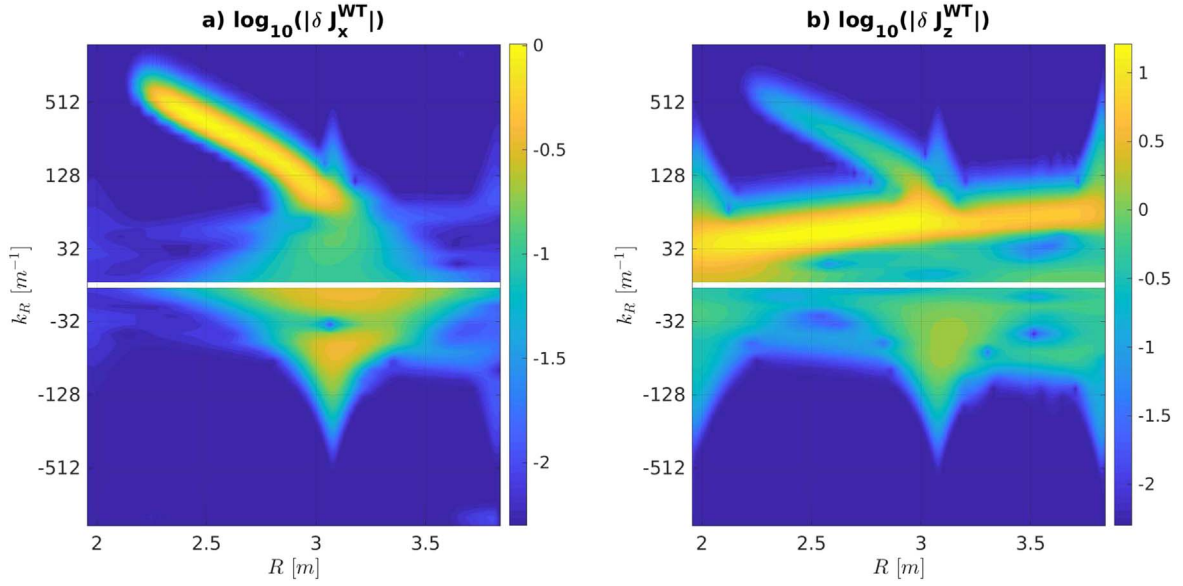


Figure 15. Absolute value of the wavelet coefficients of the correction current. (a) δJ_x and (b) δJ_z .

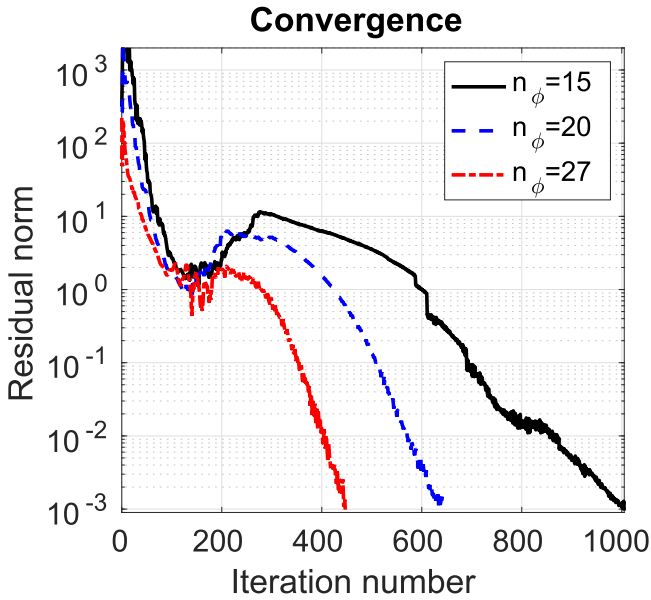


Figure 16. Residual norm (see equation (44)) evolution with the iteration number for the three toroidal mode numbers.

zone, the wavelength of the IBW becomes shorter and at some point it will become comparable to the ion Larmor radius, so that $\lambda_H \sim 1$. The consequence when the smallness assumption is broken is that the electron Landau damping becomes significantly weaker compared with an all-order FLR model, as was discussed in [41].

To evaluate equation (6) and account for the non-local response, a wavelet approach was used. The evaluation can also be done with Fourier bases, however, the Morlet wavelet approach has two advantages over the Fourier approach. The first is that Morlet wavelets are localized in space while having a narrow wave number content. Morlet wavelets are therefore suitable for describing waves in inhomogeneous media. The second advantage is that the wavelet transform

does not require a periodic function on a finite grid. Fourier decomposed functions are required to be periodic in order to avoid the Gibbs phenomenon. Instead, wavelets have the problem of producing edge artifacts, which occur when Morlet wavelets are close to the boundaries. In this work, the issue is solved with the matched layer technique (see section 3.5), which is computationally inexpensive.

The main challenge of the iterative wavelet FE scheme is the number of iterations required to achieve convergence, which makes the numerical method slow. The number of iterations appears to correlate with the number of wavelengths in the correction current $\delta \mathbf{J}_{ind}$. In [27], a wavelet spectral method was used to solve the wave equation and study fast wave heating in a toroidal plasma, which could account for non-local response in the parallel dispersion (i.e. the up- and downshift in the parallel wave number). The wave equation was solved by describing all differential operators in wavelet space, including the curl-curl operator, i.e. solving the implicit equation

$$(\mathbf{I} + \chi_0)E^{(n+1)} = \frac{c^2}{\omega^2} \nabla \times \nabla \times E^{(n)} - \delta \hat{\chi} E^{(n)}, \quad (45)$$

where χ_0 is the cold susceptibility tensor. The required number of iterations to achieve convergence was ~ 100 . In [24], a similar wave equation was solved, but using the iterative wavelet FE scheme. For this case, the required number of iterations to achieve convergence was reduced to ~ 10 . Hence, the slow convergence in the present model is related to the fact that the wave equation describing the propagation of the IBW is treated using wavelets. Therefore, a possibility to reduce the number of iterations is to move the lowest order FLR effects from the correction current using operator splitting and include them in the FE method, and let the correction current contain higher order FLR effects.

In FEMIC1D, the most time consuming part is the calculation of the inverse continuous wavelet transform of the

correction current (equation (40)). One approach to improve the performance of the inverse wavelet transform is to remove the redundancy in the wavelet representation of the functions, in particular, for large wavelets. For example, the discretization in the shift parameter b can be improved by using a coarser resolution for larger wavelets, while maintaining fine resolution for smaller wavelets only.

6. Conclusion

In summary, we have developed a new numerical method based on an *iterative wavelet FE* scheme, which has the capability to solve the wave equation and take into account FLR effects to all orders. To verify the method, we studied a case of one-dimensional fast wave heating at the second harmonic ion cyclotron resonance of hydrogen and study mode conversion to IBWs. Comparison with simulations performed with the TOMCAT code shows good agreement in regions where the Landau damping of the IBW is not significant. The numerical method can also account for FLR effects related to the polarization of the fast wave in the yz plane, which are caused by the $\hat{\chi}_{zy,j}$ term in the susceptibility tensor.

The main advantage of the proposed numerical scheme is that it relies mainly on the FE method, which is suitable for solving the wave equation in complex geometries. In particular, the method can use the FE method in the low-density and antenna regions in a tokamak, where spatial dispersion effects are either weak or absent. Iterative addition of spatial dispersion effects are applied locally (i.e. the plasma domain), since the correction current $\delta\mathbf{J}_{ind}$ is evaluated on the wavelet grid, which is smaller than the FE grid. Another advantage of the method is that the problem solved with the FE method does not have to be a rigorous description of the plasma response, as iterations are used to approach the rigorous description.

The main challenge of the iterative wavelet FE scheme is to reduce the number of iterations required to achieve convergence (which is left for future work). One way to achieve this is to move the lowest order FLR terms from the correction current and treat them using the FE method, and only iterate on higher order FLR terms.

Acknowledgments

We thank our colleague K Lindvall for his useful comments on the manuscript. This work has been carried out within the framework of the EUROfusion Consortium and has received funding from the Euratom research and training programme 2014–2018 and 2019–2020 under grant agreement No 633053. The views and opinions expressed herein do not necessarily reflect those of the European Commission.

Appendix. Susceptibility tensor in wavelet space

A.1. Higher order derivatives of the Morlet wavelet

The daughter wavelets (from section 3.1) are given by

$$\psi_{ab}(x) = \frac{1}{\sqrt{|a|}} c_\sigma \pi^{-1/4} e^{-\frac{x^2}{2a}} (e^{i\sigma X_{ab}} - \kappa_\sigma), \quad (\text{A.1})$$

where $X_{ab} = (x - b)/a$ is introduced for brevity. Using the product rule for derivatives, the k :th derivative of the daughter wavelet can be written as

$$\begin{aligned} \frac{d^k}{dx^k} \psi_{ab}(x) &= \frac{1}{\sqrt{|a|}} c_\sigma \pi^{-1/4} \\ &\sum_{l=0}^k \binom{k}{l} \left(\frac{d^l}{dx^l} e^{-\frac{x^2}{2a}} \right) \left(\frac{d^{k-l}}{dx^{k-l}} (e^{i\sigma X_{ab}} - \kappa_\sigma) \right). \end{aligned} \quad (\text{A.2})$$

Using the recurrence relation for Hermite polynomials [38], it is possible to Taylor expand $\text{He}_n(x + y)$ and obtain the relation

$$\text{He}_n(x + y) = \sum_{k=0}^n \binom{n}{k} x^{n-k} \text{He}_k(y), \quad (\text{A.3})$$

which in turn can be used to evaluate equation (A.2). We obtain

$$\begin{aligned} \frac{d^k}{dx^k} \psi_{ab}(x) &= \frac{1}{a^k} \left[\text{He}_k(i\sigma - X_{ab}) \right. \\ &\left. + \frac{\kappa_\sigma}{e^{i\sigma X_{ab}} - \kappa_\sigma} [\text{He}_k(i\sigma - X_{ab}) - \text{He}_k(-X_{ab})] \right] \psi_{ab}(x). \end{aligned} \quad (\text{A.4})$$

A.2. Integrating using the Binomial theorem

Using the binomial theorem, computing the inverse Fourier transform and using the result from the previous section, it is possible to show that

$$\begin{aligned} \mathbf{I}_{ab}(x) &= \frac{1}{2\pi} \int_{k_x} \sum_{p=0}^{\infty} \frac{\left(k_x - \frac{\sigma}{a}\right)^p}{p!} \frac{\partial^p \hat{\chi}_j}{\partial k_x^p} \bigg|_{k_x = \frac{\sigma}{a}} \hat{\psi}_{ab}(k_x) e^{ik_x x} dk_x \\ &= \sum_{p=0}^{\infty} \frac{1}{p!} \frac{\partial^p \hat{\chi}_j}{\partial k_x^p} \bigg|_{k_x = \frac{\sigma}{a}} \sum_{k=0}^p \binom{p}{k} i^{-k} (-1)^{p-k} \left(\frac{\sigma}{a}\right)^{p-k} \frac{d^k}{dx^k} \psi_{ab}(x) \\ &= \sum_{p=0}^{\infty} \frac{i^p}{p!} \frac{1}{a^p} \frac{\partial^p \hat{\chi}_j}{\partial k_x^p} \bigg|_{k_x = \frac{\sigma}{a}} \left[\text{He}_p(X_{ab}) + \frac{\kappa_\sigma}{e^{i\sigma X_{ab}} - \kappa_\sigma} [\text{He}_p(X_{ab}) - \text{He}_p(X_{ab} + i\sigma)] \right] \psi_{ab}(x). \end{aligned} \quad (\text{A.5})$$

Usually, κ_σ is very small, so for low orders of p , the second term can be neglected. In that case, we obtain

$$\mathbf{I}_{ab}(x) = \sum_{p=0}^{\infty} \frac{i^p}{p!} \frac{\text{He}_p(X_{ab})}{a^p} \frac{\partial^p \hat{\chi}_j}{\partial k_x^p} \Bigg|_{k_x = \frac{\sigma}{a}} \psi_{ab}(x). \quad (\text{A.6})$$

ORCID iDs

P Vallejos  <https://orcid.org/0000-0003-4343-6325>

T Johnson  <https://orcid.org/0000-0002-7142-7103>

R Ragona  <https://orcid.org/0000-0002-3225-5732>

B Zaar  <https://orcid.org/0000-0002-3280-2361>

References

- [1] Stix T 1992 *Waves in Plasmas* (New York: American Institute of Physics)
- [2] Swanson D 2003 *Plasma Waves* 2nd edn (Bristol: Institute of Physics Publishing)
- [3] Brambilla M 1998 *Kinetic Theory of Plasma Waves* (Oxford: Oxford University Press)
- [4] Melrose D and McPhedran R 1991 *Electromagnetic Processes in Dispersive Media* (Cambridge: Cambridge University Press)
- [5] Brambilla M and Krucken T 1988 *Plasma Phys. Control. Fusion* **30** 1083
- [6] Dumont R J *et al* 2005 *Phys. Plasmas* **12** 042508
- [7] Brambilla M and Krucken T 1988 *Nucl. Fusion* **23** 1813
- [8] ITER Physics Expert Group on Energetic Particles, Heating and Current Drive and ITER Physics Basis Editors 1999 *Nucl. Fusion* **39** 2495
- [9] Perkins F W 1977 *Nucl. Fusion* **17** 1197
- [10] Porkolab M 1994 *AIP Conf. Proc.* **314** 99–127
- [11] Brambilla M and Bilato R 2006 *Nucl. Fusion* **46** S387
- [12] Dumont R 2009 *Nucl. Fusion* **49** 075033
- [13] Lamalle P U 1994 LPP ERM/KMS Brussels report no 101 generalisation theorique non locale et etude numerique tridimensionnelle du couplage daune antenne ICRH a un plasma de tokamak *PhD Dissertation* Universite de Mons
- [14] Popovich P, Cooper W A and Villard L 2006 *Comput. Phys. Commun.* **175** 250
- [15] Mellet N *et al* 2011 *Comput. Phys. Commun.* **182** 570
- [16] Villard L, Brunner S and Vaclavik J 1995 *Nucl. Fusion* **35** 1173
- [17] Jaeger E F *et al* 2002 *Phys. Plasmas* **9** 1873
- [18] Vallejos P *et al* 2019 *Nucl. Fusion* **59** 076022
- [19] Sauter O and Vaclavik J 1992 *Nucl. Fusion* **32** 1455
- [20] Sauter O and Vaclavik J 1994 *Comput. Phys. Commun.* **84** 226–42
- [21] Pletzer A, Phillips C K and Smithe D N 2003 *AIP Conf. Proc.* **694** 503
- [22] Meneghini O *et al* 2009 *Phys. Plasmas* **16** 090701
- [23] Green D L and Berry L A 2014 *Comput. Phys. Commun.* **185** 736
- [24] Vallejos P *et al* 2018 *J. Phys.: Conf. Ser.* **1125** 012020
- [25] Walker H and Ni P 2011 *SIAM J. Numer. Anal.* **49** 1715
- [26] Vallejos P *et al* 2016 *J. Phys.: Conf. Ser.* **775** 012016
- [27] Vallejos P *et al* 2017 *EPJ Web Conf.* **157** 03059
- [28] Hellsten T *et al* 2014 *J. Phys.: Conf. Ser.* **561** 012010
- [29] Hellsten T *et al* 2014 *41st EPS Conf. on Plasma Physics (Berlin, Germany, 23–27 June)* P2.060
- [30] Ashmead J 2012 *Quanta* **1** 58
- [31] Morlet J *et al* 1982 *Geophysics* **47** 203–21
- [32] Morlet J *et al* 1982 *Geophysics* **47** 222–36
- [33] Van Eester D and Koch R 1988 *Plasma Phys. Control. Fusion* **40** 1949
- [34] Smithe D N 1989 *Plasma Phys. Control. Fusion* **31** 1105
- [35] Vaclavik J and Appers K 1987 *Plasma Phys. Control. Fusion* **29** 257
- [36] Daubechies I 1992 *Ten Lectures on Wavelets* (Philadelphia, PA: SIAM: Society for Industrial and Applied Mathematics)
- [37] Jordan D *et al* 1997 *Rev. Sci. Instrum.* **68** 1484
- [38] Abramowitz M and Stegun I 1965 *Handbook of Mathematical Functions with Formulas, Graphs and Mathematical Tables* (New York: Dover Publications)
- [39] Su H, Liu Q and Li J 2012 *WSEAS Trans. Signal Process.* **8** 169–79
- [40] Brislawn C M 1996 *Appl. Comput. Harmon. Anal.* **3** 337–57
- [41] Van Eester D and Lerche E 2013 *Plasma Phys. Control. Fusion* **55** 055008
- [42] Fuchs V, Ko K and Bers A 1981 *Phys. Fluids* **24** 1251
- [43] Messiaen A *et al* 2010 *Nucl. Fusion* **50** 025026
- [44] Zhang J H 2017 *Nucl. Fusion* **57** 066030
- [45] Stix T H 1975 *Nucl. Fusion* **15** 737